Calibration of DEM material parameters to simulate stress-strain behaviour of unsaturated soils during uniaxial compression

Jan De Pue[a,*], Gemmina Di Emidio[b], R. Daniel Verastegui Flores[c], Adam Bezuijen[b], Wim M. Cornelis[a]

[a] Department of Environment, Ghent University, Ghent, Belgium
[b] Department of Civil Engineering, Ghent University, Ghent, Belgium
[c] Geotechnical Division, DMOW, Flemish Government, Belgium

A B S T R A C T

Discrete element method (DEM) is an appealing technique to simulate soil deformation. However, the calibration of the material parameters in the model remains challenging due to the high computational cost associated with it. In this study, the stress-strain relation of 125 unsaturated soil samples was simulated using DEM and material parameters were calibrated with Kriging. The Young's modulus and friction angle were found to be the most sensitive DEM material parameters, and they had a significant correlation with the bulk density, clay content and water content of the undisturbed soil samples. The DEM simulation showed that the deformation process was a combination of elastic and plastic processes, also at low stresses. Further improvement such as the coupling with (and calibration of) a fluid dynamics model might allow to more accurately simulate the dynamic behaviour of unsaturated soil compression.

1. Introduction

Soil compaction of cultivated soils is considered one of the main challenges in soil management. External mechanical stress on soils due to wheeling or tillage causes soil deformation and reduction of the pore space, which affects water and solute transport, aeration, nutrient availability and crop productivity (Soane and Van Ouwerkerk, 1995; Hamza and Anderson, 2005; Alaoui et al., 2011; Keller et al., 2013).

Amongst the methods to simulate soil deformation, the Discrete Element Method (DEM) is an appealing technique. A DEM model consists of a granular assembly of particles which interact through contact forces. Depending on the contact model used, contact forces can include elasticity, friction and cohesion. At larger scale these interactions result in a network of force chains and complex macroscopic elastoplastic behaviour (Cundall, 2001; O'Sullivan, 2011). This versatile concept can be used to simulate the mechanical behaviour of soil under various conditions, as in shearing tests (Kim et al., 2012), penetrologger tests (Kotrocz et al., 2016), wheel-surface interaction (Smith et al., 2014) and soil tillage interaction (Shmulevich., 2010). In earlier studies DEM has demonstrated its value to simulate uniaxial and triaxial compression tests, in particular for dry sands and concrete. The propagation of deformation and damage, as well as the stress-strain relation predicted by the DEM showed good agreement with theoretical expectations and experimental results (Thornton, 2000; Camborde et al., 2000; Widuliński et al., 2009; Zhao and Guo, 2013; Kozicki et al., 2014).

Calibration of such models is a challenging task. DEM simulations are typically associated with a high computational cost, leading often to a (comprehensive) trial-and-error approach rather than using gradient-based algorithms (Coetzee, 2017). This forward-based methodology is restricted by parameter dimensionality and inefficient to execute for a large number of repetitions. Alternatively, some ensemble-based methods have been proposed. Benvenuti et al. (2016) used an artificial neural network-based method to estimate the DEM contact law parameters of sinter ore fine. Cheng et al. (2018) introduced a sequential quasi-Monte Carlo approach. Evolutionary optimization methods have proven their merits to optimize complex models (Gobeyn et al., 2017) and have been applied to DEM as well (Do et al., 2018). Rackl and Hanley (2017) used a Kriging-based procedure to calibrate the model and optimize the time step in the model.

The macroscopic mechanical behaviour of soils is determined by various soil properties, amongst which particle grain size distribution, particle shape and roughness, organic matter content, bulk density, water content and matric potential (Mouazen et al., 2002; Cho et al., 2006; Tang et al., 2009; Keller et al., 2011). Likewise, the material

parameters used in a DEM simulation should be related to those properties. However, little research has been committed to this hypothesis, since the calibration of DEM is exception rather than the rule and because most studies which simulate soil mechanical behaviour with DEM are restricted to a single soil type.

In this study, 126 undisturbed soil samples were collected in fields with varying land use and texture, and were subjected to uniaxial compression. The latter was simulated with DEM and the material parameters for each soil sample were calibrated using Kriging. Additionally, soil properties of the samples were determined in the lab. This allows to investigate the relation between the optimized DEM parameters in this simulation and measured soil properties. In summary, the objectives of this study were (1) to evaluate the accuracy of the simulated uniaxial compression with calibrated DEM material parameters, and (2) to investigate the relation between soil properties and DEM material parameters.

2. Materials and methods

2.1. Soil samples and lab analysis

Undisturbed soil samples were collected in agricultural fields in Flanders, covering the six major soil textural classes (i.e. Sand (Z), Loamy Sand (S), Sandy Loam (P), Sandy Silt Loam (L), Silt Loam (A) and Clay (E)), in three classes of contrasting land use (i.e. pasture, headland (labeled as "Head") and infield position of arable land (labeled as "Centre")) and at two depths (40 cm and 70 cm). The goal of this sampling strategy was to encompass a wide range of soil texture and structure (i.e. degree of soil compaction). For each sample location, three samples (height: 20.0 mm and diameter: 63.5 mm) were subjected to uniaxial compression at different preset matric potentials (i.e. −70 hPa, −100 hPa and −330 hPa). The resulting dataset consists of 126 ($7 \times 3 \times 2 \times 3$) analysed samples.

Sand, silt and clay content of each sample was determined with the sieve-pipette method of De Leenheer (1959), and organic carbon content with the Walkley and Black (1934) method. The initial dry bulk density and water content was determined by weighing the samples prior to the uniaxial compression test and afterwards, after they were oven-dried at 105 °C.

The results of the texture analysis are shown in Fig. 1. The maximum measured clay content was 0.33 kg/kg. Average organic carbon content and bulk density values per land use and sampling depth are given in Table 1. The organic carbon content was found to be significantly lower at 70 cm than at 40 cm sampling depth, whereas no significant difference was found between land uses according to a

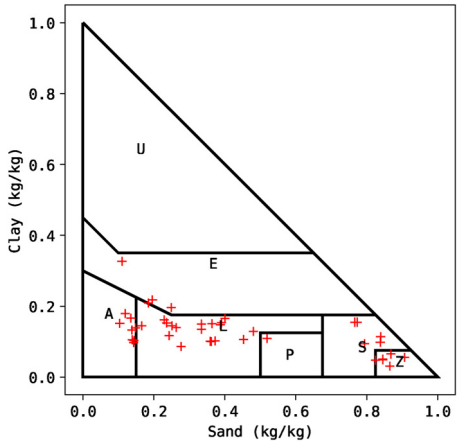

Fig. 1. Texture of the sample locations, plotted on the Belgian texture triangle. Texture class symbols are Sand (Z), Loamy Sand (S), Sandy Loam (P), Silt Loam (A), Clay (E) and Heavy Clay (U).

Table 1
Median organic carbon content (OC), bulk density (BD) and ζ in the soil samples per land use class and sampling depth. Superscript letters indicate that no significant difference (Mann–Whitney rank sum test $p < 0.05$, with Bonferroni correction) was found between the groups with the same letter.

	Land use					
	Pasture		Cropland centre		Cropland head	
Depth (cm)	40	70	40	70	40	70
OC (% kg/kg)	0.39^{ac}	0.19^{bc}	0.27^{ac}	0.22^{abc}	0.31^{ac}	0.12^{abc}
BD (kg/m^3)	1507^{abe}	1527^{abce}	1640^{bcde}	1520^{abe}	1648^{cde}	1602^{abcde}
ζ (kPa)	169.5^{abc}	146.0^{abc}	218.9^{ab}	162.8^{ac}	263.2^{ab}	250.4^{abc}

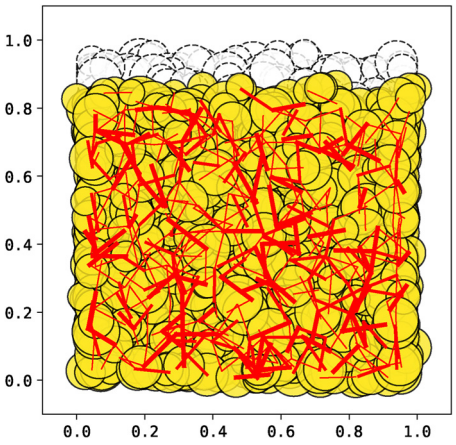

Fig. 2. Side view of the 3D DEM model for uniaxial compression samples of the training ensemble at $\sigma = 2000$ kPa. The yellow spheres are the DEM elements, the dashed lines show the initial state of the model, and the red lines show the force chain network (the 25% strongest normal force interactions, wider lines represent stronger interactions). (For interpretation of the references to color in this figure legend, the reader is referred to the web version of this article.)

Table 2
Distributions of DEM parameters used to create training data ensemble.

Parameter	Mean	Std
$\log_{10}(E)$ (Pa)	8.5	0.8
ν (–)	0.4	0.2
ϕ (rad)	$0.2\frac{\pi}{2}$	$0.1\frac{\pi}{2}$
$\log_{10}(a_n)$ (Pa)	5.0	1.0
$\log_{10}(a_t)$ (Pa)	5.0	1.0

Mann–Whitney rank sum test of this dataset. The bulk density of the soil at 40 cm depth at the headland and infield position of arable land was significantly higher compared to that in the pasture. No significant difference was found between land use classes for the soil at 70 cm depth. The soil was significantly denser at 40 cm than at 70 cm depth in the infield position of the arable land, whereas no such difference was found in the other land use classes.

For uniaxial compression, the samples were placed in an oedometer with lateral confinement and subjected to eight load stresses of 15, 29, 57, 113, 224, 447, 895 and 1786 kPa for 30 min each. Vertical displacement was measured with 0.001 mm resolution (or 5×10^{-5} m/m strain resolution) at 1 Hz sample rate. The precompression stress (ζ) was determined as the stress at the point of maximum log normal stress (σ)–strain (e) slope of a 4th degree polynomial regression of the $\log \sigma - e$ relationships. For a stable estimation of ζ it was necessary to ensure linear behaviour of the spline at the boundaries of the measurements by adding additional linearly extrapolated points. The method is inspired by Lamandé et al. (2017), who developed a

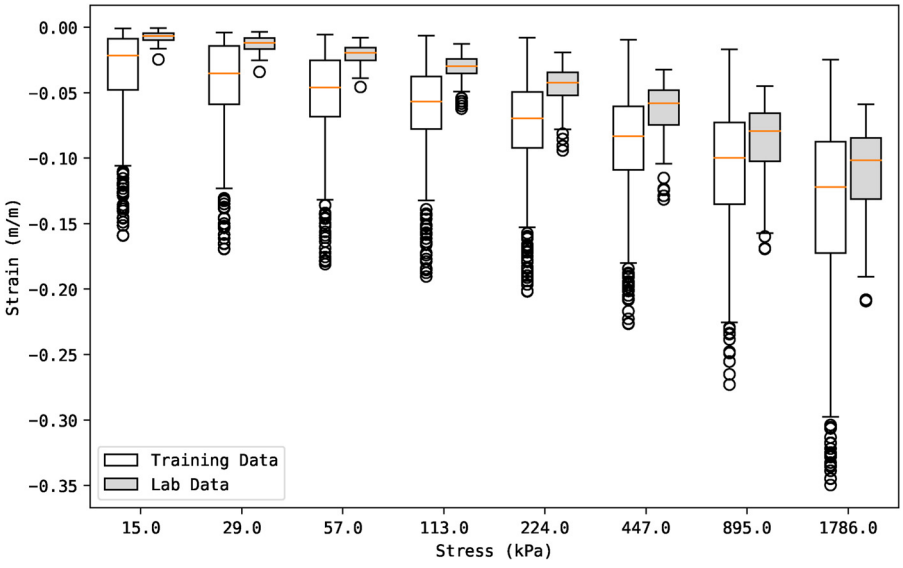

Fig. 3. Distribution of lab measured and training ensemble simulated strain at 15, 29, 57, 113, 224, 447, 895 and 1786 kPa. The boxes indicate the range between the upper and lower quartile of each distribution, and the red line shows the median. The whiskers extend from the minimum to the maximum value, and the outliers are shown with dots. (For interpretation of the references to color in this figure legend, the reader is referred to the web version of this article.)

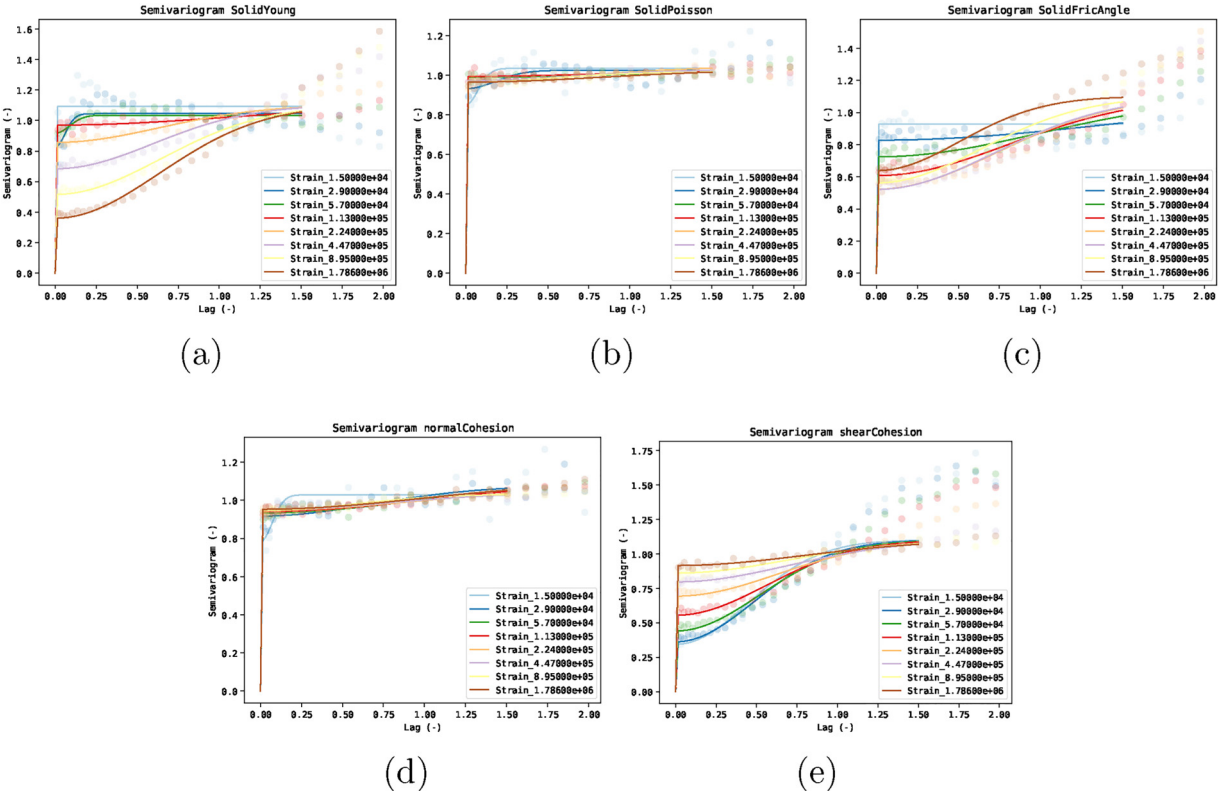

Fig. 4. Experimental (dots) and modelled (lines) semivariograms for the prediction of E (a), ν (b), ϕ (c), C_n (d) and C_t (e) with strain at 15, 29, 57, 113, 224, 447, 895 and 1786 kPa.

numerical method to find the inflection point of the stress strain relation, and was validated as a better alternative to the methods Casagrande (1936) or Gregory et al. (2006) by De Pue et al. (2019b).

The strain at 1786 kPa ranged from 0.06 m/m to 0.21 m/m, with a median of 0.10 m/m. One lab sample was omitted from the dataset because the strain at 1786 kPa was not measured. The median pre-compression stress was 196.7 kPa. The median ζ per land use and sample depth is given in Table 1. A significantly higher ζ (Mann–Whitney rank sum test $p < 0.05$, with Bonferroni correction) was found at 40 cm sampling depth in the infield position of the arable fields, compared to at 70 cm depth.

2.2. Discrete element method

Since it was first conceived by Cundall and Strack (1979), the DEM concept has not changed a lot. The numerical explicit procedure at every timestep consists of (1) detection of the interaction between particles (collision detection), (2) determination of the associated forces using a contact law, and (3) integration of the forces and Newtonian motion equations, and update the particle state (i.e. position). We used the YADE (Yet Another Discrete Element) framework to create a DEM model with spherical particles and a cohesive-frictional contact law (Šmilauer et al., 2015; Bourrier et al., 2013).

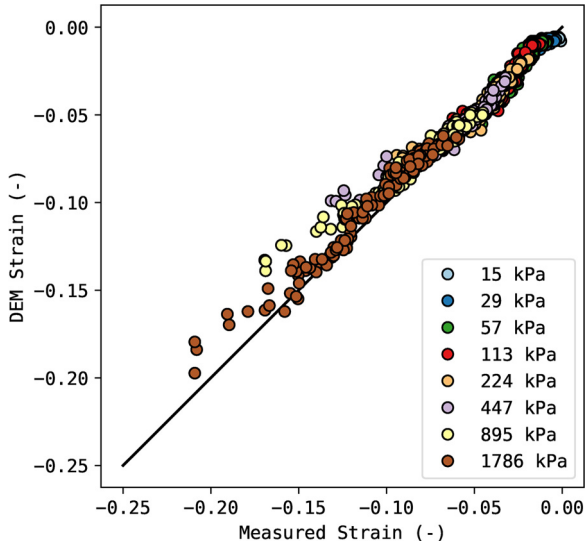

Fig. 5. Validation of the stress/strain simulation with calibrated DEM material parameters for 125 samples. RMSE was 6.70×10^{-3} m/m and Pearson r was 0.99.

Table 3
Median ζ and calibrated DEM material parameters per land use, sampling depth, texture class, matric head and texture × matric head interaction. The number of averaged samples is given between the brackets in the first column. Superscript letters indicate that no significant difference ($p > 0.05$, with Bonferroni correction) between the groups with the same letter. Rows with * symbol are evaluated with a Wilcoxon signed rank test (i.e. pairwise) instead of a Mann–Whitney rank test (i.e. independent).

	E (10^8 Pa)	ν (–)	ϕ (–)	C_n (10^5 Pa)	C_t (10^6 Pa)
Grass (41)	1.41^{ab}	0.356^{a}	0.388^{a}	0.95^{ab}	0.67^{a}
Centre (42)	3.25^{abc}	0.370^{a}	0.404^{a}	1.26^{abc}	0.73^{a}
Head (42)	3.30^{bc}	0.351^{a}	0.406^{a}	1.39^{bc}	1.03^{a}
40.0 cm (62)	3.01^{a}	0.363^{a}	0.401^{a}	0.93^{a}	0.78^{a}
70.0 cm (63)	1.97^{a}	0.356^{a}	0.391^{b}	1.38^{b}	0.94^{a}
A (24)	2.08^{ac}	0.359^{a}	0.398^{ac}	1.40^{abc}	1.09^{ab}
E (12)	0.85^{bc}	0.337^{a}	0.334^{bc}	1.24^{abc}	0.76^{abc}
L (53)	3.18^{ac}	0.362^{a}	0.404^{ac}	0.93^{ab}	0.74^{bc}
P (3)	2.29^{abc}	0.353^{a}	0.394^{abc}	1.35^{abc}	0.81^{abc}
S (15)	3.10^{ac}	0.352^{a}	0.414^{ac}	0.92^{ab}	1.06^{abc}
Z (18)	3.22^{ac}	0.377^{a}	0.397^{ac}	1.72^{ac}	0.79^{abc}
−60 hPa (42) *	2.36^{a}	0.355^{a}	0.398^{a}	1.00^{a}	0.72^{a}
−100 hPa (42) *	2.25^{a}	0.364^{a}	0.395^{a}	1.36^{a}	0.75^{a}
−330 hPa (41) *	3.05^{a}	0.358^{a}	0.397^{a}	1.30^{a}	1.06^{a}
A −60 (8) *	3.57^{a}	0.365^{a}	0.400^{a}	1.24^{a}	0.73^{a}
A −100 (8) *	3.37^{a}	0.347^{a}	0.395^{a}	1.31^{a}	0.76^{a}
A −330 (8) *	1.93^{a}	0.369^{a}	0.382^{a}	1.61^{a}	1.18^{a}
E −60 (4) *	1.10^{a}	0.318^{a}	0.337^{a}	1.09^{a}	0.75^{a}
E −100 (4) *	0.80^{a}	0.345^{a}	0.295^{a}	1.48^{a}	0.66^{a}
E −330 (4) *	0.83^{a}	0.391^{a}	0.347^{a}	1.03^{a}	0.82^{a}
L −60 (18) *	2.62^{a}	0.351^{a}	0.401^{a}	0.93^{a}	0.69^{a}
L −100 (18) *	3.13^{a}	0.372^{a}	0.408^{a}	0.92^{a}	0.67^{a}
L −330 (17) *	3.89^{a}	0.357^{a}	0.398^{a}	0.95^{a}	0.90^{a}
P −60 (1) *	1.16^{a}	0.377^{a}	0.356^{a}	1.35^{a}	0.31^{a}
P −100 (1) *	2.29^{a}	0.353^{a}	0.394^{a}	1.15^{a}	0.81^{a}
P −330 (1) *	3.34^{a}	0.303^{a}	0.419^{a}	1.57^{a}	1.20^{a}
S −60 (5) *	3.65^{a}	0.358^{a}	0.412^{a}	0.54^{a}	1.11^{a}
S −100 (5) *	2.04^{a}	0.356^{a}	0.415^{a}	1.63^{a}	1.03^{a}
S −330 (5) *	3.10^{a}	0.334^{a}	0.414^{a}	0.92^{a}	1.06^{a}
Z −60 (6) *	4.06^{a}	0.370^{a}	0.409^{a}	1.40^{a}	0.77^{a}
Z −100 (6) *	2.47^{a}	0.372^{a}	0.367^{a}	1.93^{a}	0.87^{a}
Z −330 (6) *	4.05^{a}	0.379^{a}	0.407^{a}	1.72^{a}	0.79^{a}

2.2.1. Contact law

For the DEM simulation of soils or dry sands, the most commonly applied contact laws are the linear spring contact law (Cundall and Strack, 1979) and the Hertz-Mindlin contact law (Hertz, 1882; Mindlin, 1949). The Hertz-Mindlin contact law accurately describes the contact between spheres, but is computationally more demanding than the linear model (Thornton et al., 2011). Furthermore, excellent results could be obtained for the simulation of elastic particle collision with the linear model as well, provided an adequate calibration of the parameters (Di Renzo and Di Maio, 2004; Thornton et al., 2011).

In addition to the two classical contact models, some specific contact models have been proposed to simulate soil mechanical behaviour, such as the hysteretic spring contact law (Walton and Braun, 1986) or the Luding contact law (Luding, 2008a). The disadvantage of these more complex models is that they come with the price of additional parameters, which complicates the calibration procedure.

An important property of (wet) soil is its cohesive behaviour. Studies have shown that the accurate simulation of soil mechanical behaviour requires the simulation of cohesion (Scholtès et al., 2009; Ucgul et al., 2015). The linear spring model can be extended to include cohesion, resulting in the linear cohesive-frictional law as proposed by Bourrier et al. (2013) (see below). In this study, the linear cohesive-frictional law was used. It has the advantage that its computational demand is limited and that it requires a limited set of material parameters. However, the presented calibration methodology can be applied with any contact model.

The linear cohesive-frictional law determines the normal force F_n, shear force F_t and Mohr Coulomb plasticity condition F_{tmax} at the interaction between two particles. It uses five material parameters: the Young modulus (E), the Poisson ratio (ν), the friction angle (ϕ), the normal cohesion (C_n) and the shear cohesion (C_t). The forces were calculated as follows (with the convention of positive tensile forces):

$$F_n = \min(k_n u_n, a_n) \tag{1}$$

$$F_t = k_t u_t \tag{2}$$

$$F_{\text{tmax}} = F_n \tan(\phi) + a_t \tag{3}$$

with k_n and k_t the normal and shear stiffness, u_n the normal overlap between particles, u_t the shear displacement, ϕ the friction angle, and a_n and a_t the normal and shear adhesion. Stiffness and adhesion at interaction between elements was calculated as follows:

$$k_{nj} = 2E_j R_j, \quad \text{for } j = 1, 2 \tag{4}$$

$$k_{t_j} = \nu_j k_{n_j}, \quad \text{for } j = 1, 2 \tag{5}$$

$$k_i = \frac{k_{i1} k_{i2}}{k_{i1} + k_{i2}}, \quad \text{for } i = n, t \tag{6}$$

$$a_i = C_i \min(R_1, R_2)^2, \quad \text{for } i = n, t \tag{7}$$

where $j = 1, 2$ denotes the two particles in the interaction, R_j is the radius, E_j the Young modulus, ν_j the Poisson ratio of the particle, C_n is the normal cohesion and C_t the shear cohesion. When two particles with different materials interact, the maximum ϕ, C_n and C_t are used. For clarity: the DEM material properties are not the same as macroscopic soil mechanical parameters, although they share the same name (e.g. Young modulus, Poisson ratio). The DEM material parameters are used in the model to calculate interaction forces between particles, whereas macroscopic soil mechanical parameters describe the bulk elastoplastic behaviour of the soil (Stránský and et al., 2010). Cohesive interactions were active without overlap, when the normal distance between the particles was smaller than 1.5 times their radii. To allow energy dissipation at the quasi-static equilibrium state, a global viscous damping factor of 0.4 is introduced (Hentz, 2003; Šmilauer et al., 2015). A numerically stable simulation was achieved by setting the time step size equal to the minimum time needed for the elastic p-wave to travel

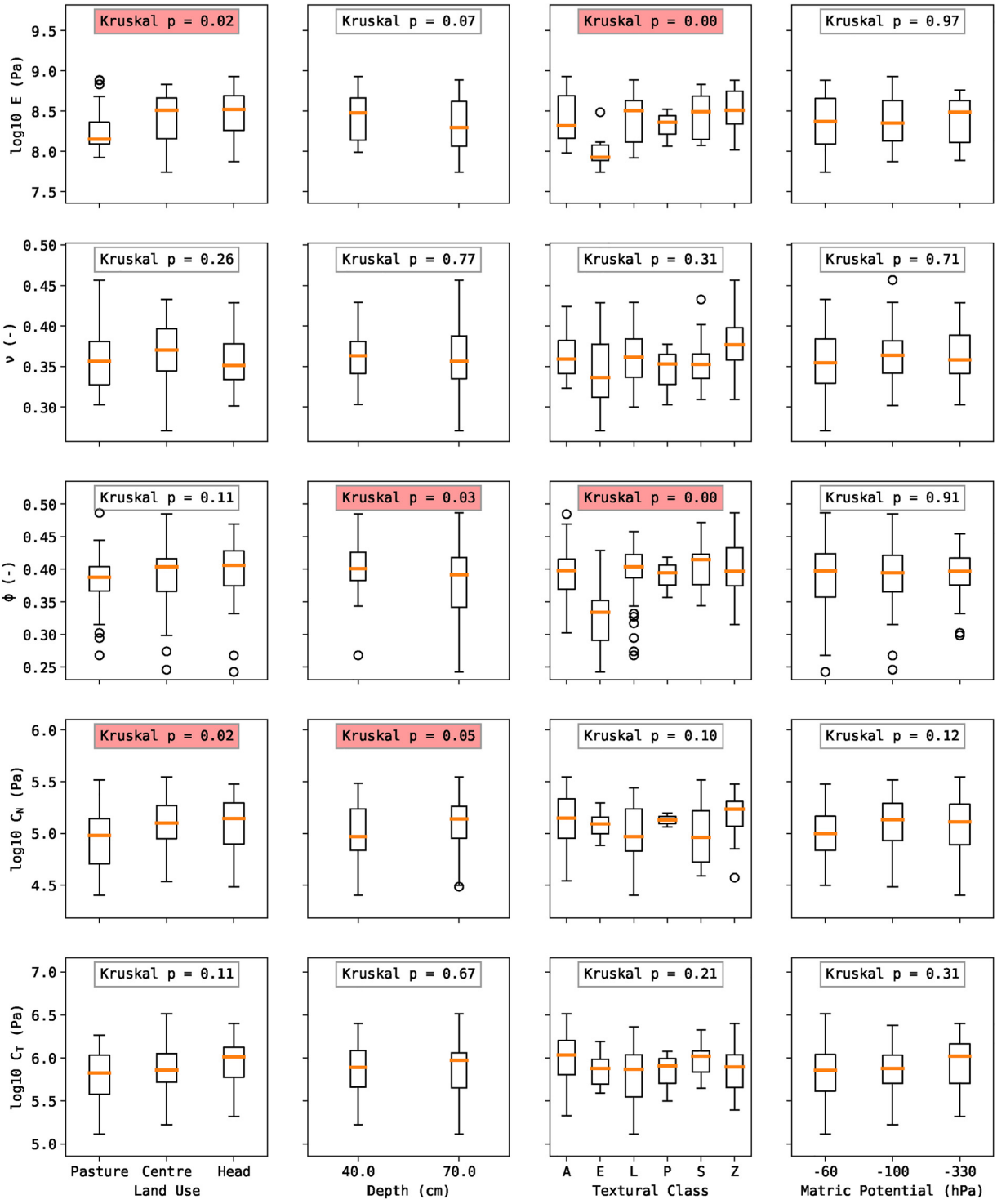

Fig. 6. Distribution of the DEM material parameters according to different land use classes, sampling depth, texture class and matrix potential. Significant interactions (Kruskal–Wallis test $p < 0.05$) are highlighted in red. (For interpretation of the references to color in this figure legend, the reader is referred to the web version of this article.)

across a particle. This is determined by the stiffness, density and size of the particles (Šmilauer et al., 2015; Burns and Hanley, 2017). It was verified that the simulated stress-strain relation was insensitive to the cohesive interaction radius and the global viscous damping coefficient (not shown here).

2.2.2. *Uniaxial compression*

For the simulation of uniaxial compression, a polydisperse sample of spherical particles was created by gravitational deposition. The contact law as described in the previous section was used, the model does not include suction or pore fluid dynamics. The rotational degrees of freedom were blocked to emulate the behaviour of non-spherical particles (Oda et al., 1982; Salot et al., 2009; Coetzee, 2017). This could also be achieved by including rotational resistance in the model, but this approach was avoided since this would add at least one additional parameter to be calibrated. It was verified that particle rotation was of

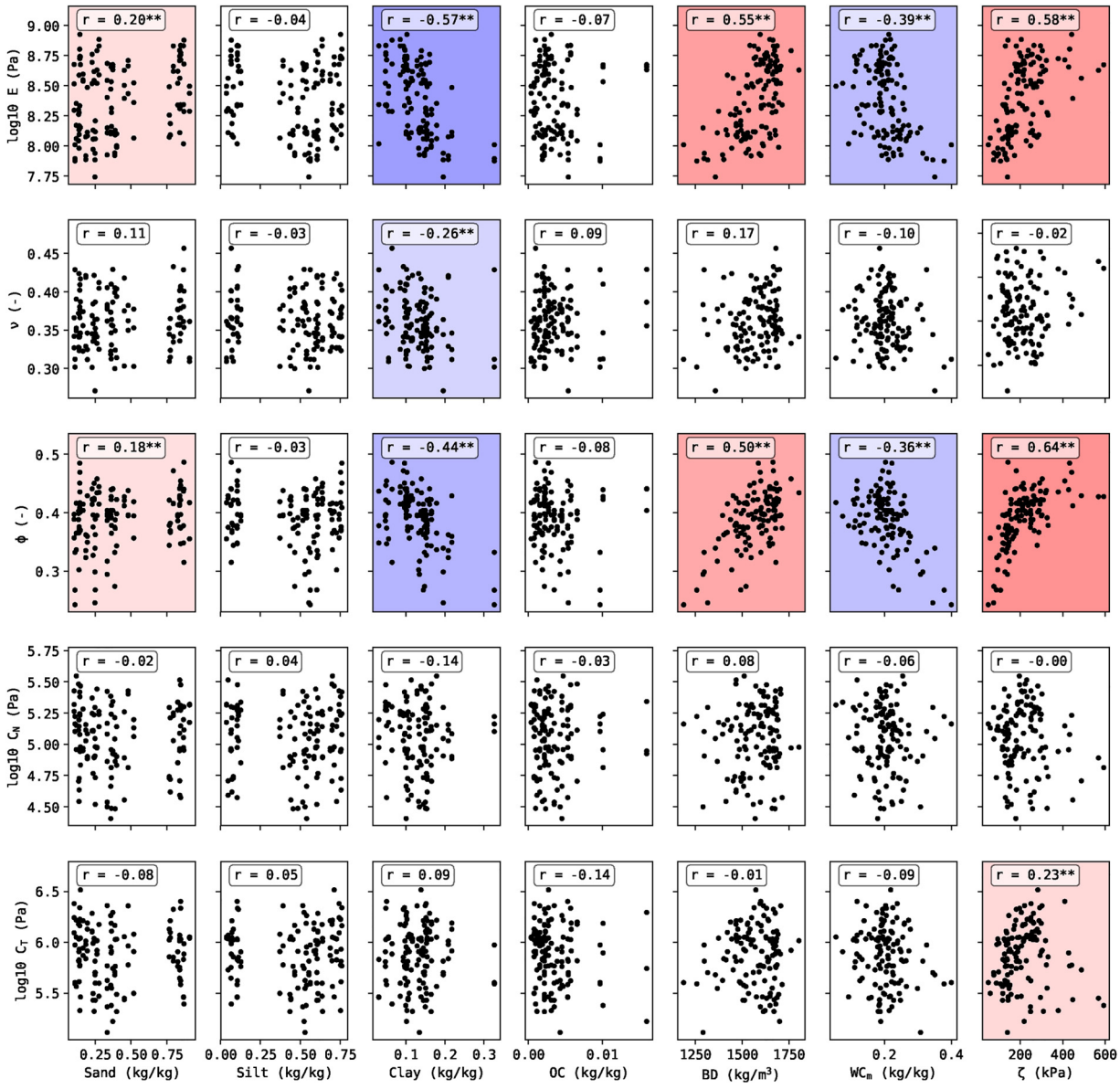

Fig. 7. Spearman rank correlation matrix for the calibrated DEM parameters, ζ values and lab soil properties. The asterix indicates that the correlation is significant (0.05 significance level).

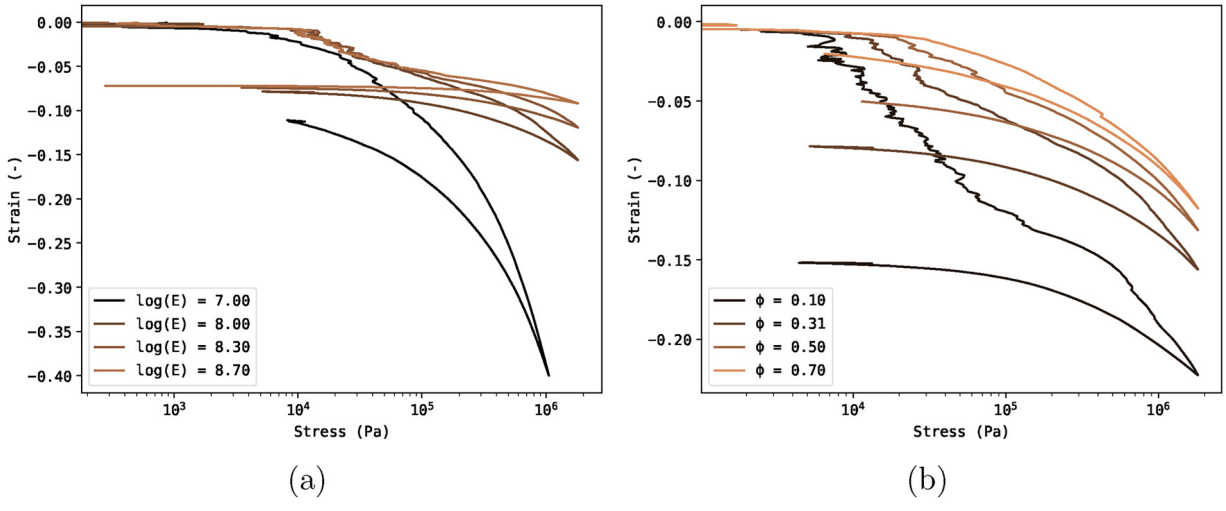

Fig. 8. Simulated stress-strain relation with (a) varying E ($\phi = 0.31$ rad) and (b) varying ϕ ($E = 1 \times 10^8$ Pa).

limited influence on the stress-strain relation (not shown here), so it was justifiable to block the rotational degrees of freedom in this model. Evidently, this implies that the resulting calibrated material parameters can only be used in other models where it is justified to block the particle rotations.

The sample was subjected to a uniaxial load of 2000 kPa and restricted to zero strain at the two remaining axes. The simulation had periodic boundary conditions and gravity was neglected. This allowed to reduce the computational cost (increase the time step) by up-scaling the model without affecting the stress-strain relation (Lommen et al., 2014). The particle density was set to 2600 kg/m^3 (it was verified that this had no effect on the stress-strain relation). A soil volume of 1.0 m × 1.0 m × 1.0 m and a mean particle radius of 0.055 m (± 30%) resulted in a loose packing (porosity = 0.47) of ~700 particles. The strain in repeated simulations with random packings showed a standard deviation of 0.0045 m/m, which was deemed acceptable. Further reduction in particle radius would lead to simulations with a lower uncertainty, but are unlikely to alter the calibration results. Fig. 2 shows a rendered representation of the particles and force chains of a DEM simulation. From the simulated stress-strain relation, the strain of the model was determined at eight stresses corresponding to the lab measurements (15, 29, 57, 113, 224, 447, 895 and 1786 kPa).

2.3. Calibration

The calibration procedure used the macroscopic stress-strain relation to estimate DEM parameters (i.e. a bulk calibration method, Coetzee, 2017). A training ensemble was created by latin hypercube sampling of the parameter space. E, a_n and a_t were sampled from a lognormal distribution, whereas ν and ϕ were sampled from a normal distribution. Table 2 provides the specifications of each distribution, which were chosen to cover values commonly encountered in literature for DEM simulations with soil. ϕ and ν were forced to be within boundaries: $0.01 < \nu < 0.99$ and $0.01\frac{\pi}{2} < \phi < 0.99\frac{\pi}{2}$. 959 samples were generated; for each of them a uniaxial compression up to 2000 kPa was simulated with DEM and 760 samples were retained after omitting samples with $e_{2000\,kPa} < -0.35$ (which is problematic for periodic boundary conditions and unrealistic). Fig. 3 shows that the simulated strains covered the lab observations.

Kriging, aka Gaussian process regression, is a data mining technique which is best known as a geostatistical interpolation method (Cressie, 1992). It is also used for the interpolation of non-spatial variables, in particular as a meta-modelling method in various applications (Simpson et al., 2001; Bessa et al., 2017). Rackl and Hanley (2017) developed a workflow for an efficient calibration of a DEM model, using a combination of Kriging, multiobjective optimisation and iterative DEM calibration. In this study a more simplistic inverse prediction approach was used; the bulk response variables (i.e. strain at the 8 stresses) were used to predict the material parameters by Kriging. The semivariogram values of each predictor were modelled with the Gaussian semivariogram model. It was assumed that the mean of the response variable is unknown and locally stationary, allowing to use the ordinary Kriging method. More in-depth details on the Kriging algorithm are given in De Pue et al. (2019a).

3. Results

The DEM material parameters (i.e. E, ν, ϕ, C_n and C_t) of each sample were estimated by Kriging. For each of them, a set of semivariogram models was created based on the training dataset (Fig. 4). The strains at the eight stresses were the predictor variables. E and ϕ had a low semivariance (or inversely: a high covariance) to the strain at high stress, whereas C_t was mainly determined by the strain at low stress. It was also evident that ν and C_n have an overall high semivariance, meaning that the simulation of strains under uniaxial compression was rather insensitive to both material parameters.

The DEM simulation was executed with the calibrated material parameters for 125 samples and compared to lab measurements. Validation results are shown in Fig. 5. The overall mean error (ME) was 2.97×10^{-3} m/m, root mean square error (RMSE) was 6.70×10^{-3} m/m (min 2.09×10^{-3} m/m and max 20.64×10^{-3} m/m) and Pearson r was 0.99.

An overview of the resulting calibrated parameters is given in Table 3. Interactions between the DEM material parameters according to land use, sampling depth, texture class and matric potential were evaluated with a Kruskal–Wallis non-parametric analysis of variance, shown in Fig. 6. A Mann–Whitney rank test and Wilcoxon signed rank were used to evaluate the differences between the classes, as indicated in Table 3. The Kruskal–Wallis test indicates significant differences in E, ϕ and C_n due to land use, depth and texture. The calibrated E and C_n for samples from pasture land were significantly lower than for samples from the headland, and the samples at 40 cm depth have a significantly higher ϕ. A significantly lower E and ϕ was found for texture class E (clay) compared to most other texture classes and no significant differences due to matric head were found, even within each texture class.

Furthermore, the correlation between the soil properties and calibrated DEM parameters was tested with the Spearman rank correlation test. The resulting correlation matrix is shown in Fig. 7. Clay content, bulk density, water content and ζ showed a significant correlation with E and ϕ. Additionally, there was a trend that clay content had a stronger correlation with E and ϕ at less negative matric potentials (i.e. $r = 0.68$ and 0.59 at −60 hPa, and $r = 0.46$ and 0.32 at −330 hPa), whilst the correlation between bulk density and E was the highest at −330 hPa ($r = 0.70$). ν, C_n, and C_t had no significant or a poor correlation with any of the soil properties.

4. Discussion

Validation of the calibrated DEM model demonstrated that Kriging is an accurate method to predict the material parameters. The ensemble-based technique allowed an efficient calibration for 125 soil samples, and provides some insight in the sensitivity of the stress-strain relation to the material parameters. From the semivariogram (Fig. 4) it is evident that the simulated strain at high stress is sensitive to E and ϕ, whereas the deformation at low stress is more sensitive to C_t. The contact model shows that C_t determines F_{tmax}, independent of F_n. Consequently, the shear displacement at low stress is mainly determined by this parameter. However, uniaxial tests are not ideal for estimating all DEM parameters, as illustrated by the insensitivity of the uniaxial strain to ν and C_n. Including the unloading cycle, performing a triaxial test or combination with additional soil mechanical tests would probably allow a better calibration of the DEM parameters.

Still, the calibrated E and ϕ showed a significant correlation with measured soil properties (sand and clay fraction, bulk density and water content). Significant differences were found between classes of land use, sampling depth, and texture, all of which were expected to influence the soil structure and stress-strain behaviour (Soane and Van Ouwerkerk, 1994). In a DEM simulation of soil compaction, a low E results in a soft, elastic material, where the stress is converted to deformation and potential energy. The results in this study correlate this behaviour to wet clay soils, with a low bulk density and ζ. On the other hand, a high ϕ indicates a stiff material with a high yield stress and a force network with straight force chains and more lateral force transmission (Muthuswamy and Tordesillas, 2006). Here, this is correlated to dry soils with low clay content, high bulk density and high ζ, or soils with a higher degree of compaction.

E and ϕ were found to be correlated, yet they control different phenomena in the model. As illustrated with simulations, shown in Fig. 8, E determines the elastic behaviour of the soil, whereas ϕ controls the plastic shear failure. According to classic soil mechanics within the continuum approach, the soil deformation process in a uniaxial compression test is divided in two parts: an initial elastic, or recoverable

phase, followed by the non-recoverable plastic phase (Casagrande, 1936; Terzaghi, 1951). However, in the DEM simulations here it seems that the plastic phases occurs simultaneously with the elastic phase. Initially the elastic forces are transmitted through force chains. Once they fail, the particles reorganize to a more stable packing and new force chains are formed. This restructuring from a loose packing to a dense packing is not recoverable (i.e. plastic). It continues until the maximum packing density is achieved, and the bulk material behaves perfectly elastic. This is in accordance to experimental observations by Dexter. (1975), Arvidsson and Keller (2004) and Naveed et al. (2016), who observed plastic deformation of soils also at low stress levels (i.e. below ζ) and stress transmission through force chains. As other micromechanical studies have demonstrated, the shear strength of a granular materials is determined by the stability of these force chains. The key mechanism for plastic failure of soils is buckling of force chains, rather than interparticle frictional sliding (Tordesillas et al., 2009; Hanley et al., 2015). The deformation of soil should be regarded as a non-affine process, in which plastic and elastic processes occur simultaneously (Berli, 2001; Keller et al., 2011).

The stress-strain relationship was simulated accurately with the calibrated parameters, but the dynamic behaviour of the soil is not realistic. An equilibrium compression state was achieved within seconds, whereas the oedometer results showed a more gradual deformation. To optimize the dynamic behaviour of the model, additional variables such as strain rate or strain rate acceleration should be considered in the optimization procedure, as well as the introduction of additional model components which determine the dynamic properties of the model. Rolling friction is frequently introduced to improve the dynamic characteristics in DEM simulations of hopper discharge or dynamic angle of repose tests (Coetzee, 2017). However, this parameter usually is related to particle shape and the consequential inhibited rotation, whereas it was verified that this had a limited impact in this model.

Soil deformation is a combination of shear failure and pore fluid dynamics (Horn, 2003), the presented model does not contain any pore fluid dynamics. A contact model including viscous forces could be used to emulate the presence of pore fluids, or the global damping coefficient could be calibrated as well (Luding, 2008b; Cheng et al., 2018). Alternatively, a more complex model which couples the DEM to a computational fluid dynamics model (CFD) could be calibrated (Derakhshani et al., 2016). The latter is a challenging task, due to the additional computational demands of such a model design and additional degrees of freedom in the parameter space. Furthermore, in absence of pore pressure measurements or other data related to the CFD, only an indirect calibration of the CFD parameters would be possible (i.e. based on the macroscopic bulk response).

5. Conclusion

The uniaxial compression of 125 undisturbed soil samples was accurately simulated with the calibrated parameters. The calibrated parameters showed a significant relation to the sampling factors, soil properties and precompression stress. E and ϕ were the most relevant DEM parameters, and showed a high correlation with clay content, bulk density, water content and ζ. The macroscopic elastic behaviour was determined by E, whereas ϕ controlled plastic failure. The calibrated parameters allowed to simulate uniaxial compression tests, but the simulation showed a low sensitivity to some parameters (i.e. ν and C_n). Additional unloading data or a combination with other tests (triaxial test, shear test) would be required to establish a parameter set which could yield accurate simulations under other boundary conditions.

The DEM simulation showed that the deformation process was a combination of elastic and plastic processes, also at low stresses. Yet, further improvement, such as including viscous damping in the contact model or the coupling with (and calibration of) CFD might allow to simulate the dynamic behaviour of unsaturated soil compression more accurately.

DEM has proven to be a suitable approach to simulate the deformation of granular media and to gain fundamental insight in the deformation of unsaturated, structured soils, but requires the specification of material parameters. This study demonstrated that Kriging is an efficient method to predict material parameters for a large number of samples.

Acknowledgements

This work was conducted within the SNOWMAN RAI-SOILCOMP project (SN04-03). The authors wish to thank Maarten Volkaert and Jan Van Der Perre for their tireless work in the lab and on the field. This work stands on the shoulders of the many who offer free, open source knowledge and tools. The authors gratefully acknowledge the work of all collaborators who developed YADE and maintain it to be a easily accessible model and thank Sci-hub for making scientific knowledge available to everyone.

References

Alaoui, A., Lipiec, J., Gerke, H., 2011. A review of the changes in the soil pore system due to soil deformation: a hydrodynamic perspective. Soil Tillage Res. 115, 1–15. Arvidsson, J., Keller, T., 2004. Soil precompression stress: I. A survey of Swedish arable soils. Soil Tillage Res. 77 (1), 85–95.

Benvenuti, L., Kloss, C., Pirker, S., 2016. Identification of DEM simulation parameters by artificial neural networks and bulk experiments. Powder Technol. 291, 456–465. Berli, M., 2001. Compaction of agricultural subsoils by tracked heavy construction machinery. ETH Zurich Ph.D. thesis.

Bessa, M., Bostanabad, R., Liu, Z., Hu, A., Apley, D.W., Brinson, C., Chen, W., Liu, W.K., 2017. A framework for data-driven analysis of materials under uncertainty: coun-tering the curse of dimensionality. Comput. Methods Appl. Mech. Eng. 320, 633–667. Bourrier, F., Kneib, F., Chareyre, B., Fourcaud, T., 2013. Discrete modeling of granular soils reinforcement by plant roots. Ecol. Eng. 61, 646–657.

Burns, S.J., Hanley, K.J., 2017. Establishing stable time-steps for DEM simulations of non-collinear planar collisions with linear contact laws. Int. J. Numer. Methods Eng. 110 (2), 186–200.

Camborde, F., Mariotti, C., Donzé, F., 2000. Numerical study of rock and concrete behaviour by discrete element modelling. Comput. Geotech. 27 (4), 225–247.

Casagrande, A., 1936. The determination of pre-consolidation load and it's practical significance. In: Proc. Int. Conf. Soil Mech. Found. Eng., vol. 3. Cambridge, MA. pp. 60.

Cheng, H., Shuku, T., Thoeni, K., Yamamoto, H., 2018. Probabilistic calibration of discrete element simulations using the sequential quasi-Monte Carlo filter. Granul. Matter 20 (1), 11.

Cho, G.-C., Dodds, J., Santamarina, J.C., 2006. Particle shape effects on packing density, stiffness, and strength: natural and crushed sands. J. Geotech. Geoenviron. Eng. 132 (5), 591–602.

Coetzee, C., 2017. Calibration of the discrete element method. Powder Technol. 310, 104–142.

Cressie, N., 1992. Statistics for spatial data. Terra Nova 4 (5), 613–617.

Cundall, P.A., 2001. A discontinuous future for numerical modelling in geomechanics? Proc. Inst. Civil Eng.-Geotech. Eng. 149 (1), 41–47.

Cundall, P.A., Strack, O.D., 1979. A discrete numerical model for granular assemblies. Géotechnique 29 (1), 47–65.

De Leenheer, L., 1959. Werkwijzen van de analysen aan het centrum voor grondonderzoek. Rijkslandbouwhogeschool Gent, Ghent, pp. 60–61.

De Pue, J., Botula, Y.-D., Nguyen, P.M., Van Meirvenne, M., Cornelis, W.M., 2019a. Introducing kriging as data mining algorithm for pedotransfer functions: evaluation for temperate and tropical soil datasets. Journal of Hydrology (submitted for publication).

De Pue, J., Di Emmidio, G., Cornelis, W.M., 2019b. Functional evaluation of the various calculation methods for precompression stress. Soil Tillage Res (submitted for publication).

Derakhshani, S.M., Schott, D.L., Lodewijks, G., 2016. Calibrating the microscopic properties of quartz sand with coupled CFD-DEM framework. Eng. Computation. 33 (4), 1141–1160.

Dexter, A., 1975. Uniaxial compression of ideal brittle tilths. J. Terramechanics 12 (1), 3–14.
Di Renzo, A., Di Maio, F.P., 2004. Comparison of contact-force models for the simulation of collisions in DEM-based granular flow codes. Chem. Eng. Sci. 59 (3), 525–541.
Do, H.Q., Aragón, A.M., Schott, D.L., 2018. A calibration framework for discrete element model parameters using genetic algorithms. Adv. Powder Technol. 29 (6), 1393–1403.
Gobeyn, S., Volk, M., Dominguez-Granda, L., Goethals, P.L., 2017. Input variable selection with a simple genetic algorithm for conceptual species distribution models: a case study of river pollution in Ecuador. Environ. Model. Softw. 92, 269–316.
Gregory, A., Whalley, W., Watts, C., Bird, N., Hallett, P., Whitmore, A., 2006. Calculation of the compression index and precompression stress from soil compression test data. Soil Tillage Res. 89 (1), 45–57.
Hamza, M., Anderson, W., 2005. Soil compaction in cropping systems: a review of the nature, causes and possible solutions. Soil Tillage Res. 82 (2), 121–145.
Hanley, K.J., O'Sullivan, C., Wadee, M.A., Huang, X., 2015. Use of elastic stability analysis to explain the stress-dependent nature of soil strength. R. Soc. Open Sci. 2 (4), 150038.
Hentz, S., 2003. Modélisation d'une structure en béton armé soumise à un choc par la méthode des éléments discrets. Université Joseph Fourier (Grenoble) Ph.D. thesis.
Hertz, H., 1882. Ueber die beruhrung fester elastischer korper. J. Reine Angew. Math. 92, 156–171.
Horn, R., 2003. Stress-strain effects in structured unsaturated soils on coupled mechanical and hydraulic processes. Geoderma 116 (1-2), 77–88.
Keller, T., Lamandé, M., Schjønning, P., Dexter, A.R., 2011. Analysis of soil compression curves from uniaxial confined compression tests. Geoderma 163 (1-2), 13–23.
Keller, T., Lamandé, M., Peth, S., Berli, M., Delenne, J.-Y., Baumgarten, W., Rabbel, W., Radjai, F., Rajchenbach, J., Selvadurai, A., et al., 2013. An interdisciplinary approach towards improved understanding of soil deformation during compaction. Soil Tillage Res. 128, 61–80.
Kim, B., Park, S., Kato, S., 2012. DEM simulation of collapse behaviours of unsaturated granular materials under general stress states. Comput. Geotech. 42, 52–61.
Kotrocz, K., Mouazen, A.M., Kerényi, G., 2016. Numerical simulation of soil-cone penetrometer interaction using discrete element method. Comput. Electron. Agric. 125, 63–73.
Kozicki, J., Tejchman, J., Mühlhaus, H.-B., 2014. Discrete simulations of a triaxial compression test for sand by DEM. Int. J. Numer. Anal. Methods Geomech. 38 (18), 1923–1952.
Lamandé, M., Schjønning, P., Labouriau, R., 2017. A novel method for estimating soil precompression stress from uniaxial confined compression tests. Soil Sci. Soc. Am. J. 81 (5), 1005–1013.
Lommen, S., Schott, D., Lodewijks, G., 2014. DEM speedup: stiffness effects on behavior of bulk material. Particuology 12, 107–112.
Luding, S., 2008a. Cohesive, frictional powders: contact models for tension. Granul. Matter 10 (4), 235.
Luding, S., 2008b. Introduction to discrete element methods: basic of contact force models and how to perform the micro-macro transition to continuum theory. Eur. J. Environ. Civil Eng. 12 (7-8), 785-L 826.
Mindlin, R., 1949. Compliance of elastic bodies in contact. J. Appl. Mech., ASME 16, 259–268.
Mouazen, A.M., Ramon, H., De Baerdemaeker, J., 2002. Effects of bulk density and moisture content on selected mechanical properties of sandy loam soil. Biosyst. Eng. 83 (2), 217–224.
Muthuswamy, M., Tordesillas, A., 2006. How do interparticle contact friction, packing density and degree of polydispersity affect force propagation in particulate assemblies? J. Stat. Mech. Theory Exp. 2006 (09), P09003.
Naveed, M., Schjønning, P., Keller, T., de Jonge, L.W., Moldrup, P., Lamandé, M., 2016. Quantifying vertical stress transmission and compaction-induced soil structure using sensor mat and X-ray computed tomography. Soil Tillage Res. 158, 110–122.
Oda, M., Konishi, J., Nemat-Nasser, S., 1982. Experimental micromechanical evaluation of strength of granular materials: effects of particle rolling. Mech. Mater. 1 (4), 269–283.
O'Sullivan, C., 2011. Particle-based discrete element modeling: geomechanics perspective. Int. J. Geomech. 11 (6), 449–464.
Rackl, M., Hanley, K.J., 2017. A methodical calibration procedure for discrete element models. Powder Technol. 307, 73–83.
Salot, C., Gotteland, P., Villard, P., 2009. Influence of relative density on granular materials behavior: DEM simulations of triaxial tests. Granul. Matter 11 (4), 221–236.
Scholtès, L., Chareyre, B., Nicot, F., Darve, F., 2009. Micromechanics of granular materials with capillary effects. Int. J. Eng. Sci. 47 (1), 64–75.
Shmulevich, I., 2010. State of the art modeling of soil-tillage interaction using discrete element method. Soil Tillage Res. 111 (1), 41–53.
Simpson, T.W., Poplinski, J., Koch, P.N., Allen, J.K., 2001. Metamodels for computer-based engineering design: survey and recommendations. Eng. Comput. 17 (2), 129–150.
Šmilauer, V., et al., 2015. Reference manual. Yade Documentation, 2nd ed. The Yade Projecthttps://doi.org/10.5281/zenodo.34045. http://yadedem.org/doc/.
Smith, W., Melanz, D., Senatore, C., Iagnemma, K., Peng, H., 2014. Comparison of discrete element method and traditional modeling methods for steady-state wheel-terrain interaction of small vehicles. J. Terramechanics 56, 61–75.
Soane, B., Van Ouwerkerk, C., 1994. Soil compaction problems in world agriculture. In: Developments in Agricultural Engineering, vol. 11. Elsevier. pp. 1–21.
Soane, B., Van Ouwerkerk, C., 1995. Implications of soil compaction in crop production for the quality of the environment. Soil Tillage Res. 35 (1-2), 5–22.
Stránský, J., Jirásek, M., Šmilauer, V., 2010. Macroscopic elastic properties of particle models. In: Proceedings of the International Conference on Modelling and Simulation 2010. Prague.
Tang, A.-M., Cui, Y.-J., Eslami, J., Défossez, P., 2009. Analysing the form of the confined uniaxial compression curve of various soils. Geoderma 148 (3–4), 282–290.
Terzaghi, K., 1951. Theoretical Soil Mechanics. Chapman and Hall, Limited, London.
Thornton, C., 2000. Numerical simulations of deviatoric shear deformation of granular media. Géotechnique 50 (1), 43–53.
Thornton, C., Cummins, S.J., Cleary, P.W., 2011. An investigation of the comparative behaviour of alternative contact force models during elastic collisions. Powder Technol. 210 (3), 189–197.
Tordesillas, A., Zhang, J., Behringer, R., 2009. Buckling force chains in dense granular assemblies: physical and numerical experiments. Geomech. Geoeng. 4 (1), 3–16.
Ucgul, M., Fielke, J.M., Saunders, C., 2015. Three-dimensional discrete element modelling (DEM) of tillage: accounting for soil cohesion and adhesion. Biosyst. Eng. 129, 298–306.
Walkley, A., Black, I.A., 1934. An examination of the Degtjareff method for determining soil organic matter, and a proposed modification of the chromic acid titration method. Soil Sci. 37 (1), 29–38.
Walton, O., Braun, R., 1986. Stress calculations for assemblies of inelastic spheres in uniform shear. Acta Mech. 63 (1-4), 73–86.
Widuliński, Ł., Kozicki, J., Tejchman, J., 2009. Numerical simulations of triaxial test with sand using DEM. Arch. Hydro-Eng. Environ. Mech. 56 (3-4), 149–172.
Zhao, J., Guo, N., 2013. Unique critical state characteristics in granular media considering fabric anisotropy. Géotechnique 63 (8), 695.